NaSICON NaFe2PO4(SO4)2 revisited: insights into the crystal structure and electrochemical performance

Anastasia Grebenshchikova, Jacob Olchowka, Loïc Simonin, Mathieu Duttine, François Weill, Emmanuelle Suard, Christian Masquelier, Laurence Croguennec

NaSICON $NaFe_2PO_4(SO_4)_2$ revisited: insights on crystal structure and electrochemical performance

Anastasia Grebenshchikova[1,2,3,5,6], Jacob Olchowka[1,5,6], Loïc Simonin[3], Mathieu Duttine[1], François Weill[1,5,6], Emmanuelle Suard[4], Christian Masquelier[2,5,6,7,*], Laurence Croguennec[1,5,6,*]

[1] *Univ. Bordeaux, CNRS, Bordeaux INP, ICMCB, UMR 5026, 33600 Pessac, France*

[2] *Laboratoire de Réactivité et de Chimie des Solides (LRCS), CNRS UMR 7314, Université de Picardie Jules Verne, Hub de l'Energie, Rue Baudelocque, 80039 Amiens Cedex, France*

[3] *Université Grenoble Alpes, CEA, LITEN, DEHT, LM 17 rue des Martyrs, 38054 Grenoble, France*

[4] *Institut Laue-Langevin, 38042 Grenoble, France*

[5] *Réseau sur le Stockage Electrochimique de l'Energie (RS2E), CNRS FR 3459, Hub de l'Energie, Rue Baudelocque, 80039 Amiens, France.*

[6] *ALISTORE-European Research Institute, CNRS FR 3104, Hub de l'Energie, Rue Baudelocque, 80039 Amiens, France.*

[7] *Institut Universitaire de France, 103 boulevard Saint-Michel, F-75005 Paris, France*

* Corresponding Authors: laurence.croguennec@icmcb.cnrs.fr, christian.masquelier@u-picardie.fr

Keywords: Sodium-ion battery; positive electrode material; abundant raw materials; NaSICON structure; X-ray, neutron and electron diffraction.

Abstract

With the aim to meet the needs for positive electrode materials for Na-ion batteries, based on abundant elements, synthesis routes using two different Fe^{3+} precursors were explored for the preparation of a pure mixed phosphate-sulfate NaSICON type compound $NaFe^{3+}{}_2PO_4(SO_4)_2$ (NFPS). Interestingly, a structural model described in the *R*-3 space group is found, from careful analysis of X-ray, neutron and electron diffraction. The atoms P and S (and thus, PO_4 and SO_4 anionic groups) are statistically distributed within the polyanionic framework, with a splitting of the conventional Na2 3*b* site into two positions 3*a* and 18*f*. Na-half cells with NFPS as a positive electrode material deliver 126 mAh/g, nearly the full theoretical capacity, at cycling rate of D/30–C/30 (*i.e.* the exchange of 2 Na^+ in 30 h).

Introduction

The development of new Na-containing materials for Na-ion batteries is still a continuously ongoing and exciting research challenge, particularly in the pursuit of more sustainable and performant electrodes. For portable applications, the requirement of high energy density favors high voltage positive electrode materials, often containing expensive transition metals such as V, Co and Ni. In contrast, for stationary applications, where battery mass is less critical, cost-effectiveness becomes a key factor. Thus, the development of efficient Na-rich polyanionic positive electrode materials, based on cheap and abundant elements, represents a highly exciting task for grid energy storage. The classification of Mn as a critical raw material by EU committee in 2023 promotes research and development of new materials, based on abundant Fe. Though layered oxides theoretically represent the most high-energy density class of positive electrode materials, Fe-based α-$NaFeO_2$ possesses several unsolved issues, such as irreversible structural changes in the deintercalated state because of instability and migration of Fe^{4+} ions, which block Na diffusion pathways[1–3]. The partial cationic substitution of Mn, Co and Ni for Fe can help to minimize structural changes, thereby enhancing the stability of highly deintercalated phases[4–6]. However, while effective, this solid-state chemistry approach still relies on the use of critical elements. On the other hand, Prussian Blue Fe-based analogues are also regarded as promising sustainable materials, despite the fact that the precise control of their composition and stoichiometry, *i.e.* the amount of vacancies and structural water molecules in the final product, still remains a challenge to avoid rapid performance degradation upon electrochemical operation [7–9].

On the other side, polyanionic positive electrode materials offer stable long-term cycling and thermal stability. Among Na-based polyanionic compounds, three structural types (alluaudite, NaSICON and NVPF), have been deeply investigated in recent years[10–15]. The NaSICON framework, with the general formula $A_x(M,M')_2(TO_4)_3$, consists of lantern units made of 2 MO_6 octahedra bridged by 3 TO_4 tetrahedra (for positive electrode materials mainly M = V, Mn, Fe, Cr, Ni, Sc, Ti, Zr, etc. and T = P, S, Si, V, etc.), and forms a very stable but flexible 3D network with channels, occupied by highly mobile A (Li, Na) cations, ensuring 3D ionic conductivity. The ideal, not distorted, NaSICON structure is described in the highly symmetric *R*-3*c* (#167) space group, though distortion leads to lowering of the symmetry even to monoclinic *C*2/*c* or *P*-3 space groups for instance [16]. Considering geometric parameters such as M-O and T-O distances and their ratios as distortion parameters, Avdeev calculated that the ideal *R*-3*c* structure can, in principle, be

preserved regardless of M and T ion sizes [16]. Instead, the origin of a symmetry lowering arises from a geometric mismatch between the $M_2(TO_4)_3$ framework and the A cation size and distribution and/or ordering [16]. This precious understanding helps to design new NaSICON-structure materials with tunable properties, for example through partial cationic substitution on A sites with large cations in order to increase the bottlenecks for ionic diffusion. While cationic substitution has been already largely studied,[17–20] polyanionic substitution remains relatively unexplored, offering a promising avenue for further optimization.

Polyanionic substitution appears as an interesting strategy towards the improvement of transport properties; indeed, playing with the framework composition allows to influence the size of the diffusion channels and thus the ionic conductivity[21]. Furthermore, a synergy effect may arise, such as the combination of the superior chemical and thermal stability of phosphates with the increased $M^{n+}/M^{(n+1)+}$ redox voltage due to higher inductive effect of sulfates vs. phosphates (M--O-S vs M-O--P). As reported by Ouyang *et al.*, the difficulty to obtain mixed-polyanion NaSICON type compounds as pure phases arises from less tolerance of the polyanion site to distortion than the cation site [22]. As a result, polyanionic mixing induces strains that require, to prevent phase segregation, to be compensated by distortion of A sites, which could be the reason of symmetry lowering in these systems.

We screened the ICSD, Inorganic Crystal Structure Database, and the corresponding publications with a view to identify existing mixed polyanionic Na-based NaSICON type phases, either based on sulfate or phosphate, which possibly could be used as intercalation compounds, as summarized in **Table 1**. Different symmetry reductions are reported, from *R*-3*c* to its subgroups such as *R*-3, *C*2*/c* and even *P*2*/c* for $NaFe_2PO_4(MoO_4)_2$. Interestingly, reported mixed polyanionic NaSICON materials, except for $Na_3Zr_2(SiO_4)_2PO_4$ of monoclinic symmetry, contain only one mole of Na per formula unit. Although being reported, $Na_3Fe_2PO_4(SO_4)_2$ NaSICON-phase is not considered here due to lack of reliable structural characterization [22].

For the listed phases, we adopted Avdeev's approach to characterize their structural distortion by assessing the mismatch between the $M_2(TO_4)_3$ framework and the A cation size (for these compositions sodium), and calculating the (M-O)/(T-O) ratio using Shannon's radii. However, no clear correlation was found between these geometrical parameters and symmetry changes in the Na-based compounds compared in **Table 1**, though the lowest value for the (M-O)/(T-O) ratio of 1.18 corresponds to the least symmetric space group *P*2*/c* for $NaFe_2PO_4(MoO_4)_2$.

Table 1. List of polyanion-mixed NaSICON type structures and their corresponding average T-O distances and (M-O)/(T-O) ratios. Ionic radii for mentioned atoms[23]: $r(O^{2-})$ = 1.4 Å, $r(Si^{4+})$ = 0.26 Å, $r(P^{5+})$ = 0.17 Å, $r(S^{6+})$ = 0.12 Å, $r(As^{5+})$ = 0.335 Å, $r(Se^{6+})$ = 0.28 Å, $r(Mo^{6+})$ = 0.41 Å, $r(Fe^{3+})$ = 0.645 Å, $r(Ti^{4+})$ = 0.61 Å, $r(Mg^{2+})$ = 0.72 Å, $r(Zr^{4+})$ = 0.72 Å.

Space group	Formula	<T-O>, Å	<M-O> / <T-O>	References
R*-3*c	$Na_{0.84}Ca_{0.08}Fe_2PO_4(SO_4)_2$	1.54	1.33	[24]
	$NaTi_2(PO_4)_{1.8}(AsO_4)_{1.2}$	1.64	1.23	[25]
***R*-3*c* or *R*-3**	$NaFe_2PO_4(SO_4)_2$	1.54	1.33	[26–31]
***R*-3**	$NaFe_{1.6}V_{0.4}PO_4(SO_4)_2$	1.54	1.33	[32]
	$NaMgFe(SO_4)_{2.5}(SeO_4)_{0.5}$	1.55	1.35	[33]
	$NaMgFe(SO_4)_{1.5}(SeO_4)_{1.5}$	1.60	1.30	[33]
C*2/*c	$Na_3Zr_2(SiO_4)_2PO_4$	1.63	1.3	[34]
P*2/*c	$NaFe_2PO_4(MoO_4)_2$	1.73	1.18	[35]

Surprisingly, the mixed phosphate-sulfate NaSICON-type compound $NaFe^{3+}{}_2PO_4(SO_4)_2$ (NFPS, in the following) is described in both *R*-3*c* and *R*-3 space groups, giving space for reinvestigation. NFPS has initially been synthesized by Shiva *et al.* [26] via evaporation of solution containing $Fe_2(SO_4)_3$ and NaH_2PO_4, yielding NFPS as a main phase next to several impurities not identified by the authors. Two years later, Ben Yahia *et al.* successfully synthesized pure NFPS [25] by evaporation and annealing the mixture of $Fe(NO_3)_3{\cdot}9H_2O$, $(NH_4)_2SO_4$, $NH_4H_2PO_4$ and $NaNO_3$ precursors.[27] A modification of this procedure included modified sol-gel synthesis with microwave and ultrasound treatments [29].

Herein we report on the optimization of different synthesis routes, including ionothermal, for the preparation of pure $NaFe^{3+}{}_2PO_4(SO_4)_2$, described with a new structural model in the *R*-3 space group, with the support of neutron powder and electron diffractions, revealing a statistical distribution of PO_4^{3-} and SO_4^{2-} groups within the NaSICON framework and the splitting of the Na2 site, leading to the distribution of the Na^+ ions among two sites. Finally, nearly full theoretical capacity (126 mAh/g) was achieved for the first time for NFPS as a positive electrode material in Na-half cells at a C/30 cycling rate, opening perspectives of further optimization of that Fe-based sustainable material.

Experimental methods

Synthesis

$NaFe_2PO_4(SO_4)_2$ (NFPS) samples, denoted in the following as N, iN and AC, were obtained using 3 different synthetic routes. Iron (III) **N**itrate nonahydrate $Fe(NO_3)_3 \cdot 9H_2O$ (Sigma Aldrich, ≥ 99%) was used as the Fe^{3+}-containing precursor for **N** and **iN** samples, while Iron(III) **AC**etylacetonate $Fe(C_5H_7O_3)_3$ (Sigma Aldrich, ≥ 97%) was used for the **AC** sample. The chemical compositions and the iron content in precursors were checked through inductively coupled plasma-optical emission spectroscopy (ICP-OES).

N and AC samples were obtained via dissolution of the precursors, mixing and evaporation before final thermal treatment, while the **i**N sample was firstly subjected to **i**onothermal treatment before annealing. The synthesis procedure of N and iN samples was inspired from the work of Ben Yahia *et al* [27]. First, 1:2:2 molar stoichiometric amounts of **Na**NO_3 (Sigma Aldrich, ≥ 99%), $(NH_4)_2$**SO₄** (Sigma Aldrich, ≥ 99%) and **Fe**$(NO_3)_3 \cdot 9H_2O$ were dissolved in 15 ml of distilled water and stirred for 10 min (molar concentration of 0.33 M). Then, a second aqueous solution of 10 ml with dissolved stoichiometric amount of NH_4H_2**PO₄** (Alfa Aesar, ≥ 98%) was added to the mixture. Transparent solution was evaporated on the Petri dish, the resulting intermediate product was amorphous solid and, thus, was grinded before thermal and ionothermal treatments for N and iN samples, respectively. For the preparation of the iN sample, 500 mg of obtained powder was put into a Teflon Parr reactor with 5 ml of ionic liquid 1-Ethyl-3-methylimidazolium bis(trifluoromethylsulfonyl)imide (EMIM-TFSI; IoLiTec, ≥ 97%) and heated in a stainless-steel autoclave with an isothermal heating collar from IKA for 18 h at 220°C under constant stirring. The powder was then centrifuged with absolute ethanol and dried at 80°C. Finally, both N and iN samples were annealed at 530°C for 13 h under air.

To obtain the AC sample, two A and B aqueous solutions were mixed together and further evaporated. Solution A consisted of stoichiometric amount of concentrated H_2SO_4 (Sigma Aldrich, 95%) and iron acetylacetonate; solution B was a mixture of $NH_4H_2PO_4$ and $NaNO_3$. The resulting powder was ground and annealed at the same conditions as for the N and iN samples, at 530°C during 13 h under air.

Characterization of the three materials obtained.

X-ray powder diffraction patterns were collected using a Bruker D8 Discover diffractometer, Mo Kα radiation, operating at 50 kV and 35 mA. Samples were placed in capillaries (diameter 0.7 mm) and data was collected in the 2-30° 2θ rang (with a step size of 0.02°). The JANA2006 crystallographic computing system and the GSASII software package were used for data treatment [36,37]. Chebyshev polynomial function was used to fit the background and a pseudo-Voigt function to describe the peak profile. The crystallite size was calculated using LX and GP parameters automatically by GSASII package. The structural model described in the *R*-3 space group used for the Rietveld refinement was obtained from *R*-3*c* changing to a subgroup of lower symmetry within the POWDERCELL program [38].

The chemical composition of the samples and elemental ratio were determined by inductively coupled plasma-optical emission spectroscopy (ICP-OES) with a Varian ICP-OES 720 ES spectrometer. Powders were dissolved in a mixture of concentrated HCl and HNO_3 acids in volume ratio 1:2 and diluted by deionized water. Calibration solutions were prepared by mixing standard solutions for Na, Fe, P and S, and the wavelengths of 588.995 nm, 234.350 nm, 213.618 nm and 181.972 nm, respectively, were used.

The morphology of the particles (onto which gold was deposited) was studied using a scanning electron microscope (SEM) TESCAN VEGA. The thermogravimetric analysis (TGA) of the N sample was performed with STA 449C (TGA-DSC) Netzsch under air and in a temperature range between 33 and 900°C, with a heating rate of 5°C/min.

Electron diffraction patterns were collected using the selected area technique (SAED) on a microscope JEOL JEM-2100 (LaB_6) at 200 kV with an Orius 200D (Gatan) camera. Before being deposited on a copper TEM grid, the NFPS powder was dispersed in absolute EtOH.

The neutron powder diffraction (NPD) pattern was collected for the sample N at room temperature using the D2B High-Resolution Diffractometer (Institut Laue-Langevin, Grenoble, France) with a wavelength of 1.59 Å using Debye–Scherrer geometry. The sample N was put in an 8 mm diameter vanadium cylindrical holder. The instrumental profile function of the D2B High-Resolution NPD diffractometer was determined using $Na_2Ca_3Al_2F_{14}$ as a standard sample. Diffraction data treatment was performed using the GSASII suite software packages [37].

^{57}Fe Mössbauer spectra measurements were performed at room temperature using a constant acceleration Halder-type spectrometer operating in transmission geometry with a ^{57}Co source (embedded in Rh matrix). The calibration of the velocity scale was done with the characteristic sextet of a pure α-Fe^0 foil as reference. WinNormos software (Wissenschaftliche Elektronik GmbH) was used for refinement of the Mössbauer hyperfine parameters.

Electrode preparation and electrochemical experiments.

The synthesized N sample was ball milled with Ketjen Black (EC600JD, Lion Specialty Chem.) as a carbon additive in mass ratio 80/20 in an agate jar using a SPEX SamplePrep 8000 mixer/mill for 40 min. Then, the resulting powder was dried under vacuum overnight at 80°C and placed in an Ar-filled glove box. It was further mixed with polytetrafluoroethylene (PTFE, Sigma Aldrich) in weight ratio 95:5 in a mortar to prepare free-standing electrodes. These high-loaded (> 12 mg/cm^2) electrodes, prepared by a dry method with a view to avoid possible reactivity of dried powder with air and moisture, were assembled in CR2032-type coin cells to be tested as a working electrode with Na metal as a reference and negative electrode. The electrolyte, composed of 1 M $NaPF_6$ (Strem Chemicals; ≥ 99%) in a 1:1 (mass ratio) of ethylene carbonate and dimethyl carbonate with 2 wt% of fluoroethylene carbonate, was used. Electrochemical measurements were performed at 25°C in the voltage range 2.0 - 4.3 V vs. Na^+/Na at a cycling rate of C/30 in discharge and charge; it corresponds to the exchange of 2 Na^+/2 e^- (i.e. to a capacity of 127 mAh/g) in 30 h. Capacity retention was studied upon cycling at different discharge D-rates (from D/30 to 2D). For Galvanostatic Intermittent Titration Technique (GITT) experiments each discharge pulse was performed at a cycling rate of D/50 for 1 hour and the relaxation was then either limited in time (20 h) or as soon as the change in voltage dE/dt < 1 mV/h. When the full discharge finished after a series of successive discharge steps and relaxation periods, the same conditions were applied for charge.

Results and discussions

Synthesis strategy

Solid-state synthesis included mixing of precursors in solution, followed by evaporation and was chosen for N and AC samples to ensure better homogeneity of the mixture and to avoid segregation of phases as it could be possible in case of dry mixing/ball milling. Further exploration of thermal treatment conditions allowed to obtain a single NFPS phase with annealing time of 13 h at 530°C, *i.e.* with slightly shorter duration and lower annealing temperature than those reported in the literature (*i.e.* 15 h at 550°C)[27]. The synthesis protocol used to prepare the sample N is the simplest one to obtain NFPS. However, it requires checking for the Fe^{3+} precursor's composition, hydrated iron nitrate, before each synthesis as loss of water starts already at 50°C[38]. In order to further simplify this synthesis protocol, other inorganic Fe^{3+} precursors were considered, such as $FeCl_3$, $FePO_4$ and $Fe_2(SO_4)_3$, but without applicability, as they either introduce undesirable anion (Cl^-) or cannot ensure the targeted stoichiometry $Fe:PO_4:SO_4$ 2:1:2. On the other hand, the organometallic iron acetylacetonate $Fe(C_5H_7O_3)_3$ appears to be an interesting Fe^{3+}-containing precursor: the organic part can be decomposed and it was thus used for the synthesis of the sample AC, while concentrated sulfuric acid, $NH_4H_2PO_4$ and $NaNO_3$ were the S, P and Na precursors, respectively. After evaporation of the solution the powder was ground and annealed in the same conditions as for sample N.

One of the disadvantages of the solid-state reaction is its limited ability to control particle size and morphology, which could be crucial for performance of positive electrode materials. This is particularly important for polyanionic materials, which often suffer from limited electronic conductivity. To address this limitation, we explored the possibility of tuning the microstructure by solvo/ionothermal syntheses by using different liquid media and varying synthesis parameters such as temperature, duration, solvent ratio, etc. This strategy, previously used for the synthesis of phosphate- and sulfate-based phases in alcohols and ionic liquids, effectively yielded active materials with excellent electrochemical properties[39–43] .

Phase identification within the samples.

The three syntheses lead to samples of pure NFPS or in which NFPS was the major phase. The sample N was obtained as pure NFPS, however a small intensity peak at 17.67°2θ, which cannot be described in *R*-3*c* space group, was observed, as supported by the **Figure 1a** with qualitive

comparison of the samples, while proper structural description would be given later. This small intensity peak could not be attributed to any impurity and was detected in all samples (N, AC and iN), as reported in **Figure 1b.** For the sample AC another additional diffraction peak was barely detectable at 12.4°2θ, which could not be attributed neither **(Figure 1c)**. Finally, phase analysis of the sample iN reveals the presence of the impurity $Fe_{3.44}(PO_4)_{1.98}O_{2.08}$. Rietveld refinements were performed considering, as previously reported [26,27,29], a unit cell described in the space group *R*-3*c* for NFPS. The cell parameters determined for the three samples are ranging from 8.4138(3) Å to 8.4651(6) Å for *a* and *b* (Δa = 0.6%), from 21.98 Å to 22.06 Å for *c* (Δc = 0.4%), and from 225.2 Å^3 to 228.1 Å^3 for the cell volume per formula unit ($\Delta V/Z$ = 1.1%), with crystallite sizes ranging from 80 nm for the sample N to 230 nm for the sample iN, as compared in **Table S1.** This result raises a question of possible stoichiometry deviations in a solid solution. The cell parameters determined for sample N are the closest to the values reported by Ben Yahia *et al.*[27], while the cell parameters of samples iN and AC are close to those reported by Pinjari *et al.*[31]. Furthermore, ICP-OES conducted for samples N and AC revealed that the elemental composition is in good agreement with the targeted ratio of Na:Fe:P:S = 1:2:1:2, especially for the sample N, as reported in **Table S2.**

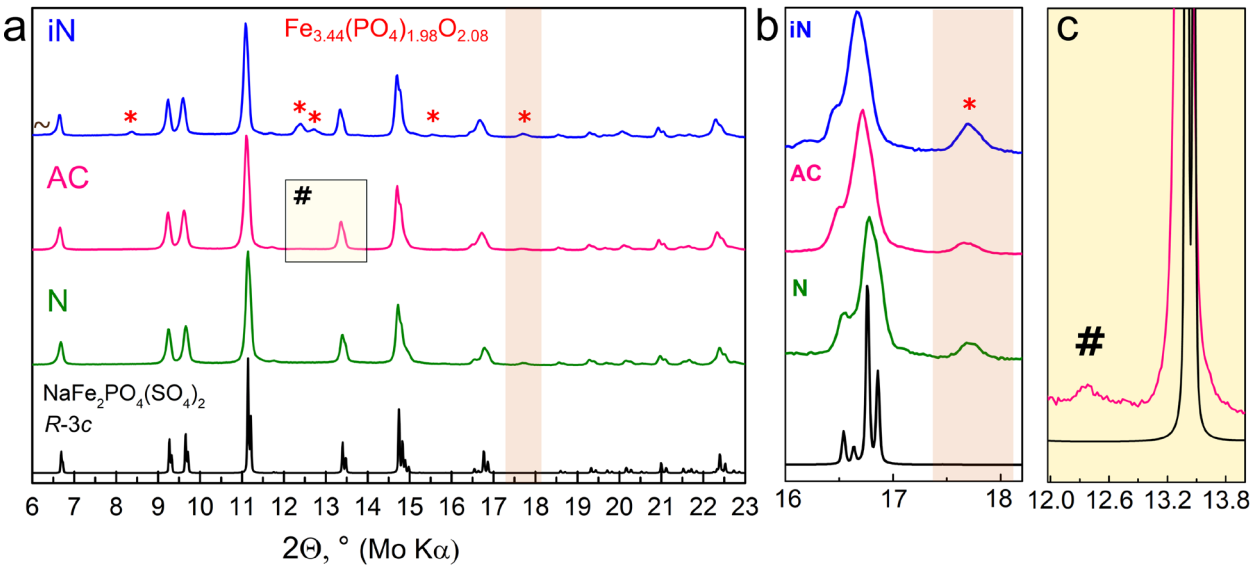

Figure 1. (a) Qualitive comparison of XRD patterns of the 3 samples of $NaFe_2PO_4(SO_4)_2$ (ICSD #264480) as the major phase, obtained from different Fe precursors and synthesis routes: iN from iron nitrate with ionothermal reaction (blue pattern) before annealing, AC from iron acetylacetonate (pink pattern) and N from iron nitrate (green pattern) by solid-state synthesis. The peak at 17.67°2θ, highlighted by beige rectangular, is not described in *R*-3*c S.G.* The iN sample contains impurity of $Fe_{3.44}(PO_4)_{1.98}O_{2.08}$ (ICSD #91189, red stars) and unidentified impurity (brown tilde). **(b)** Zoom in the 2θ angular range 16° – 18.1° to highlight a peak of small intensity at 17.67°2θ, which is overlapping with a Bragg position of $Fe_{3.44}(PO_4)_{1.98}O_{2.08}$ for the iN sample, as marked by red star. **(c)** Zoom in the 2θ angular range 11.9° – 14° of XRD pattern of the AC sample, # highlights an unidentified impurity at 12.4°2θ.

SEM images of the three samples, shown in the **Figure 2**, reveal that for direct solid-state reaction the nature of the iron precursor (iron nitrate or iron acetylacetonate for samples N and AC, respectively) has a negligible impact on the particle shape, despite a significant impact on the particle size. **Figures 2a, b** show that both samples are represented by rock-like bulky particles and characterized by wide size distribution, with bigger particles of the sample N than of AC. However, iN powder has completely different morphology that can be described as agglomerates of platelet-like primary particles of submicron size 1-5 µm (**Figure 2c**). It was already observed that remaining ionic liquid at the particle surface after ionothermal treatment prevents particle growth during subsequent annealing, possibly explaining the lower particle size[44]. By the latter result we have shown the possibility to tune morphology and particle size of NFPS by introduction of ionothermal pretreatment in EMIM-TFSI media before the annealing step. This type of morphology could ensure good electrochemical performance, though presence of impurity $Fe_{3.44}(PO_4)_{1.98}O_{2.08}$ inhibits authors' interest to study this sample and optimization of the ionothermal synthesis to obtain the pure sample is not in the scope of this paper.

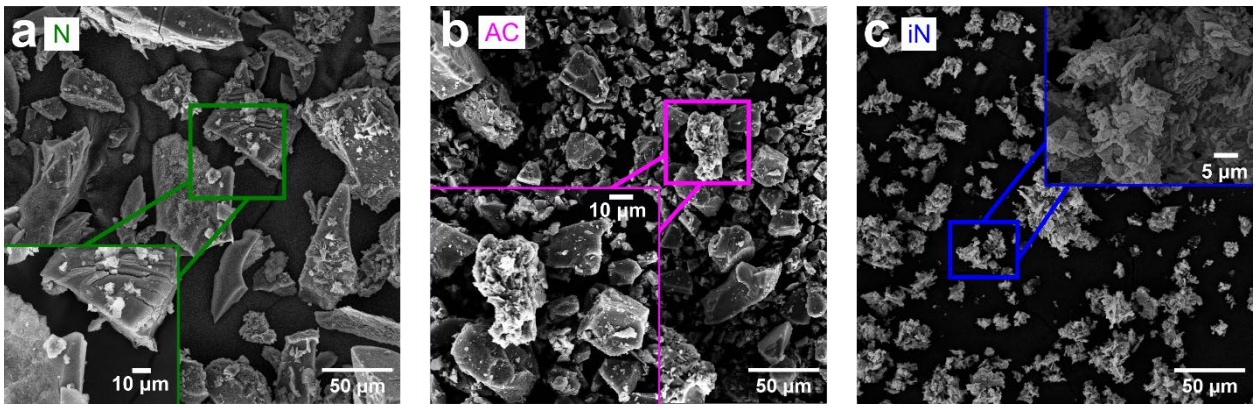

Figure 2. SEM images of the obtained samples: using a solid-state reaction **(a)** N from iron nitrate; **(b)** AC from iron acetylacetonate; and **(c)** iN from iron nitrate with ionothermal treatment before annealing.

The results of the thermogravimetric analysis of the sample N under air are presented in **Figure S1**. One can notice that NFPS starts to decompose at 600°C, with a subsequent massive weight loss (37 wt%) that occurs at 739°C, attributed to the full decomposition of the material with release of SO and SO_2 gases. It should be noted that this temperature of decomposition is slightly higher than that reported before [27] (706°C with the same heating rate under helium) and can be related to different purity of the materials.

Structural determination of NFPS

In nearly most of the previous studies $NaFe_2PO_4(SO_4)_2$ was indexed in the rhombohedral *R*-3*c* space group, but every diffraction pattern contained a non-indexed peak at ≈39°(2θ) [26,27,29] (λ_{Cu}=1.54 Å), and this peak could be indexed *303* in *R*-3 space group, as it was also recently proposed [31]. In the current work, NFPS was prepared using two different precursors and in different conditions; we found out that this *303* peak at 17.67°2θ ($\lambda K_{\alpha1}/K_{\alpha2}$(Mo) = 0.7093/0.7135 Å) was systematically observed and could not be attributed to any impurity phase. We thus considered that the choice of the space group *R*-3*c* was not appropriate to describe the structure of $NaFe_2PO_4(SO_4)_2$ and that it deserves reinvestigation.

A careful analysis of 370 NaSICON structures from the ICSD database, conducted by Avdeev [16], revealed that most of them are described into the *R*-3*c* or *R*-3 space groups, though further lowering of the symmetry to *R*32 or *C*2/*c* was also often reported. Note that this change of space group from ideal *R*-3*c* to *R*-3 results from a slight antiphase rotation of [MO_6] octahedra and [TO_4] tetrahedra around the *c*-axis and leads to the splitting of the M, A and O positions with simultaneous loss of the plane *c.* Given the significant impact of structural variations on the transport properties and ionic mobility, a proper structural description of the compounds is important, as previous similar investigations revealed the existence of different polymorphs for Na-based phosphate NaSICONs, such as $Na_3Fe_2(PO_4)_2$ and $Na_3Ti_2(PO_4)_3$ [20,45].

In the current study, we combined different diffraction techniques to revisit the crystal structure of NFPS and chose the sample N for these experiments.

Electron diffraction.

Electron diffraction (ED) is the most effective technique to assign space groups for crystallized materials and it was used here to undoubtedly discriminate *R*-3*c* vs. *R*-3 for the crystal structure description of $NaFe^{3+}{}_2PO_4(SO_4)_2$. Indeed, the presence of the *c* glide plane in *R*-3*c* gives rise to two additional reflection conditions versus *R*-3: 1) for the <h-h0l> zone axis, in addition to *h*+*l*=3*n* due to the *R* Bravais lattice, the *l*=2*n* condition must also be observed; 2) in the <000l> zone axis, *l*=6*n* is an additional condition. In ED extinctions in one direction are usually not observable because of multiple diffraction phenomena and to differentiate between the two space groups, it was therefore essential to observe the diffraction patterns along the <h-h0l> zone axis. The ED pattern collected along the [100] zone axis is shown in **Figure 3a.** Although weaker in intensity,

the reflections *003* and *021*, corresponding to *l*=2*n*+1 are clearly visible even with slight tilt, thus ruling out the possibility that $NaFe^{3+}_2PO_4(SO_4)_2$ crystallizes in the *R*-3*c* space group. This result is representative of all the crystals studied, none of them could be indexed in *R*-3*c*, or required further decrease of the symmetry, or considering extra spots due to superstructures.

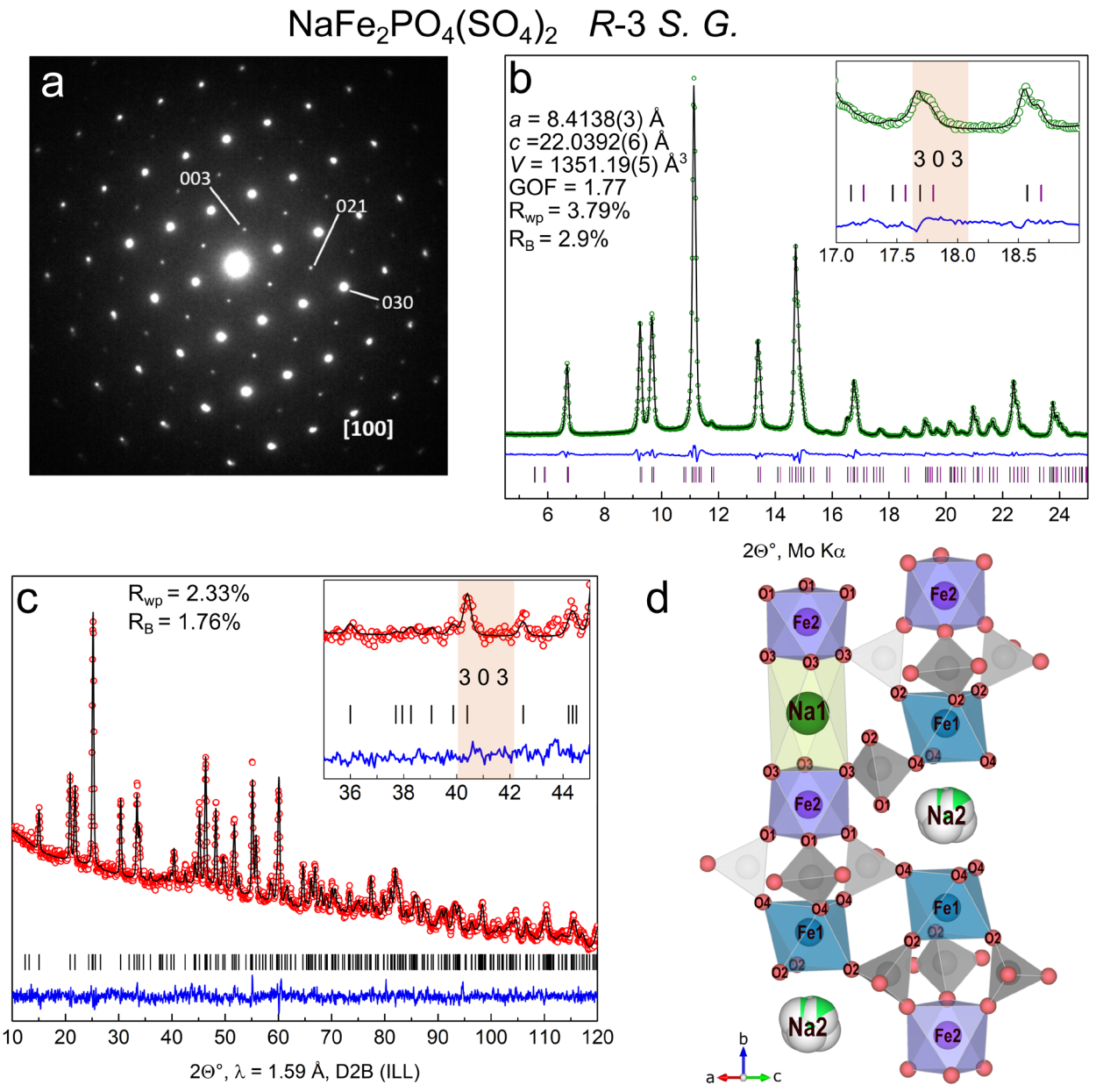

Figure 3. **(a)** Electron diffraction pattern taken at the [100] zone axis. Weak *00l* (*l*=3n) reflections indicate absence of the plane *c*. Rietveld refinements of the NFPS in *R*-3 *S.G.* from: **(b)** X-ray diffraction with the enlargement in the angular range of 17-19°2θ given in inset in to show the good fit of the controversial peak at 17.67°2; black and purple ticks correspond to $K\alpha_1$ and $K\alpha_2$ peak positions, respectively; **(c)** neutron diffraction pattern with the enlargement in the angular range of 35-45°2θ given in inset with the fit of the peak at 40.41°2θ. **(d)** Partial representation of the NFPS structure, *R*-3 *S.G.* P/SO_4 tetrahedra are shown as grey tetrahedra. Occupancy of Na2 (18*f*) site is equal to 1/6.

Neutron and X-ray powder diffraction.

Since *R*-3*c* is not the right space group to describe the structure of NFPS, simultaneous Rietveld refinement of the crystal structure from X-ray and neutron diffraction data sets was thus performed in the *R*-3 space group, clearly identified by electron diffraction. The transition from *R*-3*c* space group of higher symmetry to the *R*-3 of lower symmetry leads to the splitting of Na, Fe and O positions by 2, so that the number of atomic positions in the proposed model is 9 for the same number of formula units per unit cell, $Z = 6$. X-ray and neutron diffraction patterns after combined Rietveld refinement are shown in **Figures 4b** and **4c**, respectively. The corresponding overall refinement data, structural parameters and interatomic distances are given in **Table S3**, **Table 2** and **Table S4**, respectively. Lowering the space group symmetry to *R*-3 allowed to describe the diffraction lines, observed at 17.67°2θ (d_{303} = 2.306 Å) in the X-ray diffraction pattern and at 40.41°2θ in the neutron diffraction pattern. The (3 0 3) plane contains the P, S and Na1 atoms. It should be noted that these peaks are clearly not calculated in case of refinement in *R*-3*c S.G.*, as shown in **Figure S2 (a-b)**.

Table 2. Structural parameters of $NaFe_2PO_4(SO_4)_2$ in *R*-3 *S.G.,* determined from X-ray and neutron powder diffraction data on the sample N.

$NaFe^{3+}{}_2PO_4(SO_4)_2$						
a = 8.4138(3) Å, c = 22.0392(6) Å, V = 1351.19(5) Å^3						
Atom	Site	x/a	y/b	z/c	U_{iso}, Å^2	Occupancy
Na1	3*a*	0	0	0	0.0126(4)	1
Na2	18*f*	0.014(6)	0.046(2)	0.5096(4)	0.0126(4)	0.1667
Fe1	6*c*	0	0	0.64806(1)	0.0075(8)	1
Fe2	6*c*	0	0	0.8542(8)	0.0075(8)	1
S1	18*f*	0.2897(2)	-0.0022(3)	0.2518(2)	0.003(1)	0.667
P1	18*f*	0.2897(2)	-0.0022(3)	0.2518(2)	0.003(1)	0.333
O1	18*f*	0.0077(3)	0.1997(3)	0.1973(1)	0.006(3)	1
O2	18*f*	0.2203(3)	0.0463(2)	0.30508(3)	0.006(3)	1
O3	18*f*	0.1804(4)	0.1889(2)	0.08953(6)	0.006(3)	1
O4	18*f*	0.1490(3)	0.2021(3)	0.4106(2)	0.006(3)	1

Due to significantly different neutron scattering lengths of P and S, 5.13 fm and 2.847 fm, respectively, their distribution in the NFPS structure could be evaluated, whereas it is not possible using only XRD due to their close atomic numbers. We found out that they are disordered on a single 18*f* (x, y, z) atomic position. The refined partial site occupancies associated to P and S were found to be 0.28(2) and 0.72(2), respectively, quite close to those expected, namely, 0.333 and 0.667. Therefore, in order to reduce a number of correlations (92 refined parameters), the occupancies were fixed as 1:2 for P:S with a refined atomic displacement parameter (ADP) U_{iso} of 0.003(1) $Å^2$. The mean $(P/S)O_4$ tetrahedral environment is distorted with two longer distances (P/S)-O3 and (P/S)-O4 of 1.499(2) Å and 1.497(2) Å, respectively, and two shorter distances of (P/S)-O1 and (P/S)-O2 of 1.443(5) Å and 1.457(1) Å, respectively. It should be noted that the structural refinement gives an average description of the polyanion only, and not the local description of SO_4 on one side and PO_4 on the other, for which the average expected bond distances with oxygen are of 1.473 Å [46] and 1.531 Å [47], respectively. Note that the disorder between P and S in a single crystallographic site within this mixed-polyanion NaSICON compound probably can be explained by a small difference in ionic radii between them (0.17 Å and 0.12 Å, respectively) implying thus limited strains, induced by this mixed polyanion chemistry. On the contrary, an ordering is observed in $NaFe_2PO_4(MoO_4)_2$ [35], which occurs due to a huge difference in the ionic radii of P and Mo (0.17 Å and 0.41 Å, respectively).

Both FeO_6 octahedra are nearly similar and negligibly distorted, as reported in **Figure 4d**: $Fe1O_6$ with 3 Fe1-O2 distances of 1.983(2) Å and 3 Fe1-O4 distances of 2.001(3) Å, and $Fe2O_6$ with 3 Fe2-O1 distances of 1.990(3) Å and 3 Fe2-O3 of 2.002(2) Å. The average Fe-O bond distances are 1.992(2) Å and 1.996(3) Å, respectively, which is in line with awaited distance of 2.015 Å [48]. BVS values are 3.2(3) for Fe1 and 3.16(3) for Fe2, in good agreement with a trivalent oxidation state for iron.

A transition from *R*-3*c* to *R*-3 *S.G.* leads to the splitting of the 6*b* Na position into the two independent 3*a* and 3*b* positions. However, our results have shown that the first Na1 site is localized as expected at the 3*a* (0,0,0) position, fully occupied. However, the second one, Na2 is split to a general 18*f* (0.014(6), 0.046(2), 0.5096(4)) position, with a refined site occupancy close to 0.1667 and U_{iso} of 0.0126(4) Å ($B_{iso} \approx 1$ $Å^2$). The localization of the second Na in the 3*b* (0,0,½) site led to a negligible occupancy (0.02 *vs.* 1 as expected) or to a huge ADP ($U_{iso} \approx 0.1$ A^2), suggesting that this special position is empty and Na atoms are "distributed" in the 18*f* position. It should be noted that simultaneous refinements from neutron and XRD data confirm the correct

localization of the Na2 site in 18*f* position, while the already suggested structural model[31] in the same *R*-3 *S.G.* locates Na2 site at 3*b*. The Na1 site is a 6-oxygen coordinated trigonal prism with a Na1-O3 distance (x 6) of 2.512(2) Å. The Na2 site is a similar 6-oxygen coordinated trigonal prism, though Na2 atom is not located in its center, with 6 different Na2-O4 distances, as could be seen from **Table S4**, though with the very close average distance of 2.52(4) Å.

In conclusion, the proposed structural model in the *R*-3 space group is perfectly consistent with the expected distances and BVS values. In addition, it allows to consider all the diffraction peaks, including the one at 17.67°2θ (Mo Kα), overlooked, or not considered up to now with a structural description in the *R*-3*c* space group. It is interesting to highlight here, as reported more in details in supplementary information (**Figure S2** and **Table S5**) that a refinement of the NPD data performed in the *R*-3*c* space group would lead to a NaSICON structure with a Na deficiency (0.67 instead of 1) and, for charge compensation, to the partial oxidation of Fe^{3+} into Fe^{4+}. This result highlights how important it is, first to combine the techniques of characterization, here electron, X-ray and neutron diffractions with chemical analyses, and then, to pay attention to small intensity peaks that can be the evidence of a more complex structure than expected.

Oxidation state of iron determined by Mössbauer spectroscopy.

In order to support the composition and structure proposed for $NaFe_2PO_4(SO_4)$, we investigated the nature of the environment and oxidation state of Fe atoms using Mössbauer spectroscopy.
The local environment of Fe atoms in $NaFe^{3+}{}_2PO_4(SO_4)_2$ was studied by analyzing a ^{57}Fe Mössbauer spectrum, collected at room temperature. The spectrum, presented in **Figure 4a**, could be fitted with one broad quadrupole doublet with δ = 0.47(1) mm/s, which is typical for six-coordinated high-spin Fe^{3+} in oxygen environment[49,50]. Isomer shift of NFPS is in a good agreement with those already reported for Fe^{3+} in oxygen-coordinated octahedral sites in pure phosphate $Na_3Fe^{3+}{}_2(PO_4)_3$ (*R*-3c *S.G.*) and pure sulfate $Fe^{3+}{}_2(SO_4)_3$ (*R*-3 *S.G.*), as can be seen in **Table 3**. To obtain the best fit, the spectrum was considered as the sum of quadrupole doublets (50 sub-spectra) with the same isomer shift, same resonance line width (0.30 mm/s), but different quadrupole splitting (QS) values, indicating that there is more than one discrete environment for Fe^{3+}. As Fe^{3+} has spherically symmetrical electron distribution ($t_{2g}{}^3e_g{}^2$), QS is strongly influenced by the electric field gradient, arising from the distribution of charge around Fe sites (local distortion of FeO_6 octahedra and distribution of first cationic neighbors). As confirmed by distances obtained from XRD and NPD refinements, both FeO_6 octahedra are found

to be rather symmetrical. Large values of quadrupole splitting could arise from differences in the local distribution of first cationic neighbors, P^{5+} and S^{6+}, the distance Fe-(P,S) ranging between 3.3 and 3.4 Å. According to stoichiometry, the most probable environment is $2PO_4^{3-}/4SO_4^{2-}$, while all the other combinations are also possible, despite less probability, such as $3PO_4^{3-}/3SO_4^{2-}$, $4PO_4^{3-}/2SO_4^{2-}$, etc. The Na distribution among the Na1 and Na2 sites also affects the distortion of Fe environments, as presented in **Figures 4b,c**. The Na1 site is fully occupied with a shorter Na1-Fe2 distance of 3.23(1) Å and a longer Na1-Fe1 distance of 4.87(2) Å. On the other hand, Fe1 is located at a short distance of about 3.1 Å from the Na2 site, partially occupied and with Na^+ distributed over 6 neighboring positions, while the Fe2-Na2 distance is much longer as close to 5 Å. In conclusion, Mössbauer spectroscopy confirms the only trivalent oxidation state of iron and, given the ratio of P/S from both ICP and neutron diffraction, the stoichiometry Na:Fe of 1:2 in $NaFe^{3+}{}_2PO_4(SO_4)_2$ and supports the structural description done in the *R*-3 space group. The distribution of local environments, observed for Fe^{3+} is attributed to disorders on both the polyanionic site (due to a statistical distribution of P/S on the 18*f* site) and the Na2 site (due to a partial occupancy 1/6 of the 18*f* site).

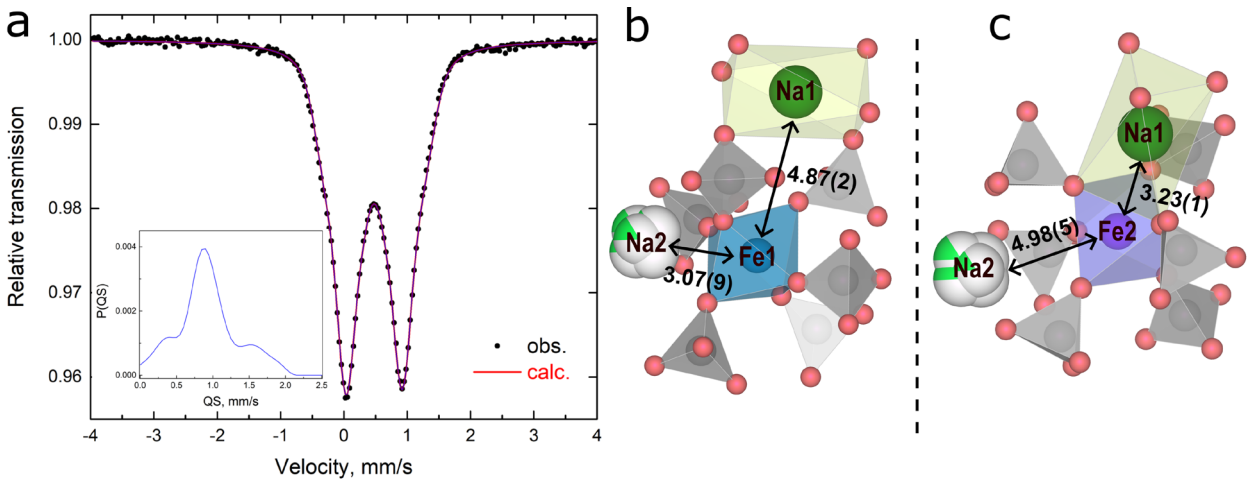

Figure 4. (a) Room temperature ^{57}Fe Mössbauer spectrum collected for $NaFe_2PO_4(SO_4)_2$. The corresponding refined hyperfine parameters are reported in **Table 3**. Inset: the distribution of the quadrupolar splitting values. Close environments of **(b)** Fe1 and **(c)** Fe2.

Table 3. Comparison of ^{57}Fe Mössbauer hyperfine parameters of NFPS with those reported in the literature (T=298K) for $Na_3Fe_2(PO_4)_3$ and $Fe_2(SO_4)_3$, where δ is the isomer shift, Δ the quadrupole splitting and Γ the line width. *mean value and standard deviation (in brackets) of the quadrupole splitting distribution. Refer to **Figure 4a** for more information on the distribution of the quadrupole splitting values.

Compound	δ, mm/s	Δ, mm/s	Γ, mm/s	Reference
$NaFe_2PO_4(SO_4)_2$	0.47(1)	0.93* [0.42]	0.30(-)	current work
$Na_3Fe_2(PO_4)_3$	0.45(1)	0.31(1)	0.28(1)	[50]
	0.451(3)	0.326(6)	0.282(5)	[51]
$Fe_2(SO_4)_3$	0.490(3)	0.0752(5)	0.395(2)	[13]

Electrochemical properties.

The electrochemical properties of the synthesized NFPS were evaluated for highly loaded electrodes (*i.e.* 15 mg/cm² of active material). The electrode material was first tested at a discharge/charge rate of D/30 and C/30 (exchange of $2e^-/2Na^+$ occurs in 30 h) in Na-half coin cells at 25°C and in the voltage range 2.0 – 4.3 V vs. Na^+/Na, as shown in **Figure 5a**.

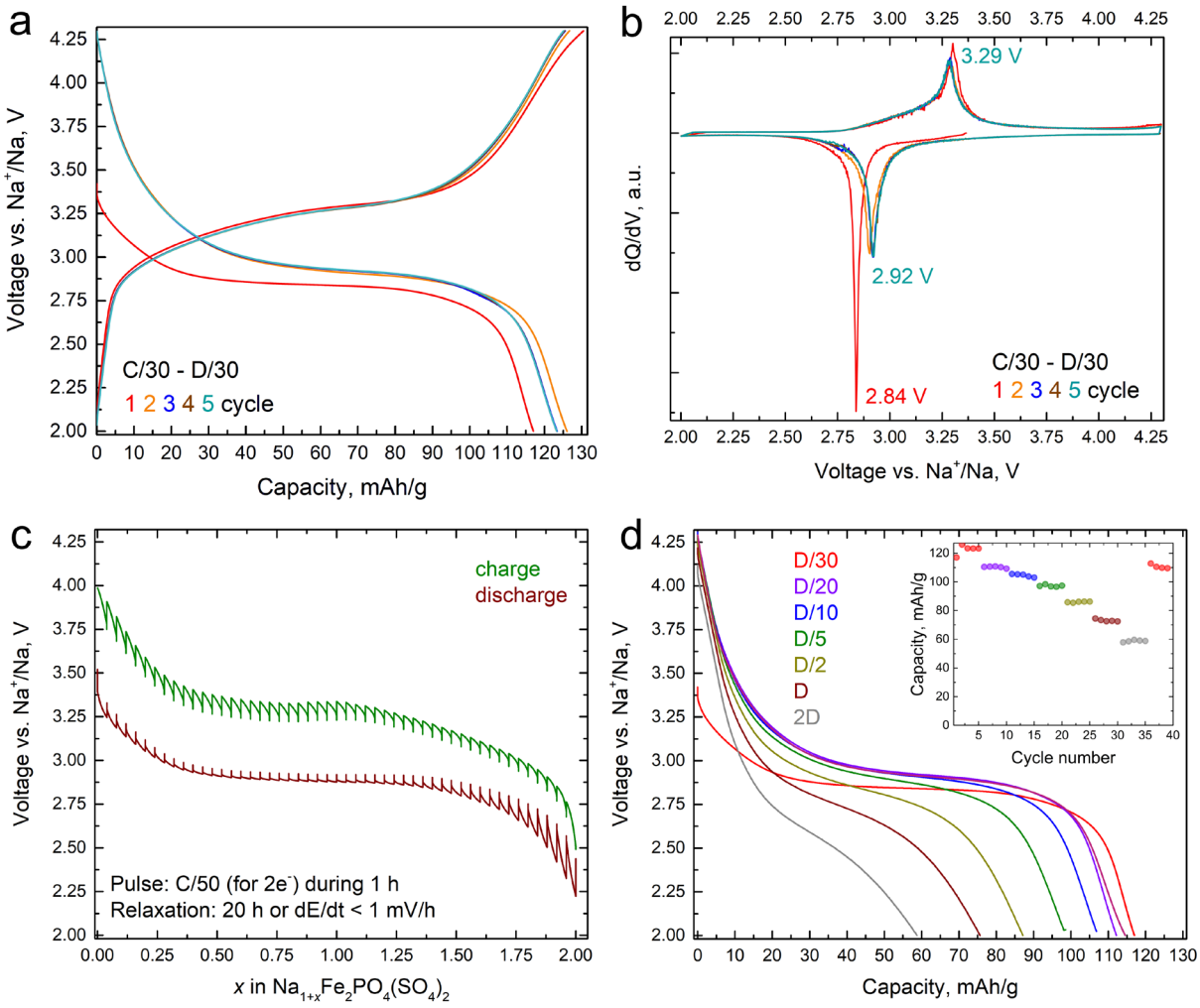

Figure 5. (a) Galvanostatic charge/discharge curves at cycling rate of D/30-C/30 in the voltage range of 2.0 V to 4.3 V vs. Na^+/Na. **(b)** Corresponding dQ/dV differential curves of the profiles presented on (a) (1^{st} cycle in red and 2^{nd} cycle in orange). **(c)** GITT curve for the 1^{st} cycle, started from discharge, confirming that 2 mol of Na^+ ions could be reversibly inserted. **(d)** Comparison of galvanostatic discharge curves obtained at different D-rates with capacity retention in inset. All the charges were performed at C/30. The 1^{st} curve at each change of regime is shown.

The galvanostatic protocol started with a discharge of the cell (Na^+ intercalation), to reduce Fe^{3+} within $NaFe^{3+}{}_2PO_4(SO_4)_2$. In the ideal case, the intercalation of 2 Na^+ mol per formula unit would provide a capacity of 127 mAh/g, and would lead to the reduction of all Fe^{3+} atoms into Fe^{2+}. During the 1^{st} discharge the material delivered 117 mAh/g and for the 2^{nd} discharge the obtained capacity was 126 mAh/g, which is nearly equal to the theoretical value. The 1^{st} charge capacity was 130 mAh/g, higher than the theoretical value, with 4 mAh/g of irreversible capacity, which can arise from electrolyte decomposition, as during next cycles it was not observed. Derivative curves at D/30-C/30 rates galvanostatic profiles in **Figure 5b** show that during the 1^{st} discharge the reduction of Fe^{3+}, assigned to a sharp distinct peak, happens at 2.84 V vs. Na^+/Na, though during following cycles this process occurs at slightly higher voltage. The dQ/dV derivative curves corresponding to the 1^{st} and 2^{nd} discharges are different, sharper for the 1^{st} and broader for the 2^{nd}, with a difference of 0.08 V between them, while the charge potential remains almost constant. After the 1^{st} discharge, the electrochemical process appears stable and reversible, with slopping charge and discharge curves and an average voltage of 3.10 V vs. Na^+/Na in good agreement with the activity of the Fe^{2+}/Fe^{3+} redox couple[27].

For the 1^{st} discharge the slopping parts at the beginning and end of the discharge curve could correspond to solid solution mechanisms, consisting in a continuous change in the structure with Na^+ intercalation, while a bi-phasic mechanism would be associated with the plateau in the middle, implying a continuous change in the proportion between two phases of fixed composition and structure. One can notice significant overvoltage of 0.44 V and 0.34 V between charge and discharge curves during 1^{st} and 2^{nd} cycles, respectively, as shown in **Figure S3**. GITT experiments were performed to investigate if the 1^{st} discharge capacity is less than that of the 2^{nd} because of kinetic or thermodynamic limitations. The results show that in conditions close to equilibrium, 2 mol of Na^+ could be inserted in NFPS structure on the 1^{st} discharge, as presented in **Figure 5c.** Despite equilibrium conditions, the observed value of hysteresis about 0.37 V was not significantly diminished. Therefore, the origin of this hysteresis seems to be intrinsic to the nature of the active material and not to electrochemical cycling conditions.

A thick free-standing electrode of NFPS with high active material loading of 15.6 mg/cm^2 (≈ 0.27 mm thick) shows good performance during cycling at high D-rates, as presented in **Figure 5d**, delivering 97 mAh/g at D/5, which is equivalent to 76% of the theoretical capacity and much higher than that already reported by Ben Yahia *et al.* (vs. 56 mAh/g and 44% of the specific capacity)[27]. After being cycled at high D-rates, such as 2D, the capacity previously obtained at D/30 is recovered up to 112 mAh/g, as shown in inset of **Figure 5d**, indicating stable cycling performance of the NFPS material.

Conclusion

Three different synthesis routes were evaluated to synthesize the NaSICON positive electrode material $NaFe^{3+}_2PO_4(SO_4)_2$, based on abundant elements. The nature of the iron precursor has a limited impact on the NFPS particle size and morphology, whereas ionothermal pretreatment step in EMIM-TFSI before annealing changes morphology and decreases particle size, though the presence of $Fe_{3.44}(PO_4)_{1.98}O_{2.08}$ impurity is observed. High purity $NaFe_2PO_4(SO_4)_2$ sample was obtained by mixing $Fe(NO_3)_3{\cdot}9H_2O$, $(NH_4)_2SO_4$, $NH_4H_2PO_4$ and $NaNO_3$ precursors in solution, prior to annealing at high temperature under air atmosphere. We revisited the structure of this phase, combining analyses of electron, X-ray and neutron powder diffraction data and determined that $NaFe_2PO_4(SO_4)_2$ crystallizes undoubtedly in the *R*-3 space group, in contrast to earlier reported *R*-3*c*. This decrease of the symmetry is caused by partial disordering of sodium ions among two sites, one being fully occupied and the other one only partially (1/6), while P and S atoms are statistically distributed on a single site. Finally, for the first time, full theoretical discharge capacity was achieved at an average voltage of 3.10 V vs. Na^+/Na, reinforcing the interest in this electrode material, composed of abundant elements only.

Supporting information: details on comparison of cell parameters of synthesized samples, ICP-OES results, TGA data, crystallographic details on refinement in *R*-3*c* space group.

Acknowledgements

Authors would like to thank Emmanuel Petit, Jérôme Kalisky, Cathy Denage, Matthew Suchomel and Stan Pechev from ICMCB for providing technical and scientific expertise and for maintenance of experimental lab equipment, X-ray diffraction, scanning electron microscopy, and chemical and thermal analyses. As part of the DESTINY PhD Program, A.G., J.O., L.S., C.M. and L.C. acknowledge the funding received from the European Union's Horizon2020 research and innovation program under the Marie Skłodowska-Curie Actions COFUND (Grant Agreement #945357). A.G. also acknowledges the funding and financial support from the CEA LITEN, as well as A.G., J.O., C.M. and L.C. that of the French National Research Agency (STORE- EX Labex Project ANR-10-LABX-76-01). The Région Nouvelle Aquitaine is thanked for the cofunding of most of the characterization equipment used in this study. Furthermore, authors also acknowledge the Institute Laue-Langevin (Grenoble, France) for neutron powder diffraction experiments on the D2B beamline with easy-access proposal EASY-1174. A.G. would like to thank Roman Shpanchenko for advice on diffraction peculiarities.

References

(1) Lee, E.; Brown, D. E.; Alp, E. E.; Ren, Y.; Lu, J.; Woo, J. J.; Johnson, C. S. New Insights into the Performance Degradation of Fe-Based Layered Oxides in Sodium-Ion Batteries: Instability of Fe^{3+}/Fe^{4+} Redox in α-$NaFeO_2$. Chem. Mater. 2015, 27 (19), 6755–6764. https://doi.org/10.1021/acs.chemmater.5b02918.

(2) Yabuuchi, N.; Yoshida, H.; Komaba, S. Crystal Structures and Electrode Performance of Alpha-$NaFeO_2$ for Rechargeable Sodium Batteries. Electrochemistry 2012, 80 (10), 716–719. https://doi.org/10.5796/electrochemistry.80.716.

(3) Li, Y.; Gao, Y.; Wang, X.; Shen, X.; Kong, Q.; Yu, R.; Lu, G.; Wang, Z.; Chen, L. Iron Migration and Oxygen Oxidation during Sodium Extraction from $NaFeO_2$. Nano Energy 2018, 47, 519–526. https://doi.org/10.1016/j.nanoen.2018.03.007.

(4) Shevchenko, V. A.; Glazkova, I. S.; Novichkov, D. A.; Skvortsova, I.; Sobolev, A. V.; Abakumov, A. M.; Presniakov, I. A.; Drozhzhin, O. A.; Antipov, E. V. Competition between the Ni and Fe Redox in the O_3-$NaNi_{1/3}Fe_{1/3}Mn_{1/3}O_2$ Cathode Material for Na-Ion Batteries. Chem. Mater. 2023, 35 (10), 4015–4025. https://doi.org/10.1021/acs.chemmater.3c00338.

(5) Kubota, K.; Asari, T.; Yoshida, H.; Yaabuuchi, N.; Shiiba, H.; Nakayama, M.; Komaba, S. Understanding the Structural Evolution and Redox Mechanism of a $NaFeO_2$–$NaCoO_2$ Solid Solution for Sodium-Ion Batteries. Adv. Funct. Mater. 2016, 26 (33), 6047–6059. https://doi.org/10.1002/adfm.201601292.

(6) Yabuuchi, N.; Kajiyama, M.; Iwatate, J.; Nishikawa, H.; Hitomi, S.; Okuyama, R.; Usui, R.; Yamada, Y.; Komaba, S. P2-Type $Na_x[Fe_{1/2}Mn_{1/2}]O_2$ Made from Earth-Abundant Elements for Rechargeable Na Batteries. Nat. Mater. 2012, 11 (6), 512–517. https://doi.org/10.1038/nmat3309.

(7) Wang, L.; Song, J.; Qiao, R.; Wray, L. A.; Hossain, M. A.; Chuang, Y. De; Yang, W.; Lu, Y.; Evans, D.; Lee, J. J.; Vail, S.; Zhao, X.; Nishijima, M.; Kakimoto, S.; Goodenough, J. B. Rhombohedral Prussian White as Cathode for Rechargeable Sodium-Ion Batteries. J. Am. Chem. Soc. 2015, 137 (7), 2548–2554. https://doi.org/10.1021/ja510347s.

(8) Song, J.; Wang, L.; Lu, Y.; Liu, J.; Guo, B.; Xiao, P.; Lee, J. J.; Yang, X. Q.; Henkelman, G.; Goodenough, J. B. Removal of Interstitial H_2O in Hexacyanometallates for a Superior Cathode of a Sodium-Ion Battery. J. Am. Chem. Soc. 2015, 137 (7), 2658–2664. https://doi.org/10.1021/ja512383b.

(9) Guo, X.; Wang, Z.; Deng, Z.; Li, X.; Wang, B.; Chen, X.; Ong, S. P. Water Contributes to Higher Energy Density and Cycling Stability of Prussian Blue Analogue Cathodes for Aqueous Sodium-Ion Batteries. Chem. Mater. 2019, 31 (15), 5933–5942. https://doi.org/10.1021/acs.chemmater.9b02269.

(10) Barpanda, P.; Oyama, G.; Nishimura, S. I.; Chung, S. C.; Yamada, A. A 3.8-V Earth-Abundant Sodium Battery Electrode. Nat. Commun. 2014, 5, 4358. https://doi.org/10.1038/ncomms5358.

(11) Trad, K.; Carlier, D.; Croguennec, L.; Wattiaux, A.; Ben Amara, M.; Delmas, C. $NaMnFe_2(PO_4)_3$ Alluaudite Phase: Synthesis, Structure, and Electrochemical Properties As

Positive Electrode in Lithium and Sodium Batteries. Chem. Mater. 2010, 22 (19), 5554–5562. https://doi.org/10.1021/cm1015614.

(12) Nanjundaswamya', K. S.; Padhi, A. K.; Goodenough, J. B.; Okadab, S.; Ohtsukab, H.; Araib, H.; Yamakib, J. Synthesis, Redox Potential Evaluation and Electrochemical Characteristics of NASICON-Related-3D Framework Compounds. Solid State Ionics 1996, 92, 1–10. https://doi.org/ 10.1016/S0167-2738(96)00472-9.

(13) Chung, S. C.; Ming, J.; Lander, L.; Lu, J.; Yamada, A. Rhombohedral NASICON-Type $Na_XFe_2(SO_4)_3$ for Sodium Ion Batteries: comparison with Phosphate and Alluaudite Phases. J. Mater. Chem. A 2018, 6 (9), 3919–3925. https://doi.org/10.1039/c7ta08606g.

(14) Yang, Z.; Li, G.; Sun, J.; Xie, L.; Jiang, Y.; Huang, Y.; Chen, S. High Performance Cathode Material Based on $Na_3V_2(PO_4)_2F_3$ and $Na_3V_2(PO_4)_3$ for Sodium-Ion Batteries. Energy Storage Mater. 2020, 25, 724–730. https://doi.org/10.1016/j.ensm.2019.09.014.

(15) Broux, T.; Fauth, F.; Hall, N.; Chatillon, Y.; Bianchini, M.; Bamine, T.; Leriche, J. B.; Suard, E.; Carlier, D.; Reynier, Y.; Simonin, L.; Masquelier, C.; Croguennec, L. High Rate Performance for Carbon-Coated $Na_3V_2(PO_4)_2F_3$ in Na-Ion Batteries. Small Methods 2018, 3, 1800215. https://doi.org/10.1002/smtd.201800215.

(16) Avdeev, M. Crystal Chemistry of NaSICONs: Ideal Framework, Distortion, and Connection to Properties. Chem. Mater. 2021, 33 (19), 7620–7632. https://doi.org/10.1021/acs.chemmater.1c02695.

(17) Gao, H.; Li, Y.; Park, K.; Goodenough, J. B. Sodium Extraction from NASICON-Structured $Na_3MnTi(PO_4)_3$ through Mn(III)/Mn(II) and Mn(IV)/Mn(III) Redox Couples. Chem. Mater. 2016, 28 (18), 6553–6559. https://doi.org/10.1021/acs.chemmater.6b02096.

(18) Singh, B.; Wang, Z.; Park, S.; Gautam, G. S.; Chotard, J. N.; Croguennec, L.; Carlier, D.; Cheetham, A. K.; Masquelier, C.; Canepa, P. A Chemical Map of NaSICON Electrode Materials for Sodium-Ion Batteries. J. Mater. Chem. A 2021, 9 (1), 281–292. https://doi.org/10.1039/d0ta10688g.

(19) Deng, Z.; Sai Gautam, G.; Kolli, S. K.; Chotard, J. N.; Cheetham, A. K.; Masquelier, C.; Canepa, P. Phase Behavior in Rhombohedral NaSiCON Electrolytes and Electrodes. Chem. Mater. 2020, 32 (18), 7908–7920. https://doi.org/10.1021/acs.chemmater.0c02695.

(20) Chotard, J. N.; Rousse, G.; David, R.; Mentré, O.; Courty, M.; Masquelier, C. Discovery of a Sodium-Ordered Form of $Na_3V_2(PO_4)_3$ below Ambient Temperature. Chem. Mater. 2015, 27 (17), 5982–5987. https://doi.org/10.1021/acs.chemmater.5b02092.

(21) Kuganathan, N.; Chroneos, A. Defect Chemistry and Na-Ion Diffusion in $Na_3Fe_2(PO_4)_3$ Cathode Material. Materials 2019, 12 (8), 1348. https://doi.org/10.3390/ma12081348.

(22) Kumar, S.; Ranjeeth, R.; Mishra, N. K.; Prakash, R.; Singh, P. NASICON-Structured $Na_3Fe_2PO_4(SO_4)_2$: A Potential Cathode Material for Rechargeable Sodium-Ion Batteries. Dalton Transactions 2022, 51 (15), 5834–5840. https://doi.org/10.1039/d2dt00780k.

(23) Shannon, R. D. Revised Effective Ionic Radii and Systematic Studies of Interatomic Distances in Halides and Chalcogenides. Acta Cryst. 1976, A32, 751. https://doi.org/10.1107/S0567739476001551.

(24) Li, S. F.; Gu, Z. Y.; Guo, J. Z.; Hou, X. K.; Yang, X.; Zhao, B.; Wu, X. L. Enhanced Electrode Kinetics and Electrochemical Properties of Low-Cost $NaFe_2PO_4(SO_4)_2$ via Ca^{2+} Doping as Cathode Material for Sodium-Ion Batteries. J. Mater. Sci. Technol. 2021, 78, 176–182. https://doi.org/10.1016/j.jmst.2020.10.047.

(25) Shimanouchi-Futagami, R.; Nishimori, M.; Nishizawa, H. Crystal Structure and Electric Conductivity of the NASICON-Related Solid Solution $NaTi_2P_{3-x}As_xO_3$ Synthesized Hydrothermally. J. Mater. Sci. Lett. 2001, 20, 1881–1883. https://doi.org/10.1023/A:1012866009766.

(26) Shiva, K.; Singh, P.; Zhou, W.; Goodenough, J. B. $NaFe_2PO_4(SO_4)_2$: A Potential Cathode for a Na-Ion Battery. Energy Environ Sci. 2016, 9 (10), 3103–3106. https://doi.org/10.1039/c6ee01093h.

(27) Ben Yahia, H.; Essehli, R.; Amin, R.; Boulahya, K.; Okumura, T.; Belharouak, I. Sodium Intercalation in the Phosphosulfate Cathode $NaFe_2(PO_4)(SO_4)_2$. J. Power Sources 2018, 382, 144–151. https://doi.org/10.1016/j.jpowsour.2018.02.021.

(28) Salame, P. H.; Devakar, M. Ultrasonically Assisted Microwave Synthesis and Electronic Transport Properties of Eldfellite, $NaFe(SO_4)_2$, a Potential Cathode Material for Sodium-Ion Batteries. Ceram. Int. 2020, 46 (18), 28844–28850. https://doi.org/10.1016/j.ceramint.2020.08.050.

(29) Salame, P.; Kotalgi, K.; Devakar, M.; More, P. Electronic Transport Properties of NASICON Structured $NaFe_2(PO_4)(SO_4)_2$: A Potential Cathode Material for Na-Ion Batteries, Synthesized Using Ultrasound-Assisted, Indirect Microwave Heating Technique. Mater. Lett. 2022, 313 (131763), 131763. https://doi.org/10.1016/j.matlet.2022.131763.

(30) Singh, M. Kr.; Bera, A. K.; Kumar, A.; Yusuf, S. M.; Dhaka, R. S. Antiferromagnetic Ordering and Glassy Nature in NASICON Type $NaFe_2PO_4(SO_4)_2$. Phys. Rev. B 2024, 109 (17), 174401. https://doi.org/10.1103/PhysRevB.109.174401.

(31) Pinjari, S. D.; Dutta, R. C.; Chen, S.; Mudavath, P.; Huang, X.; Bell, J.; Bhatia, S. K.; Nanjundan, A. K.; Gaddam, R. R. Site-Selective Mg-Doping Regulated Charge Storage in $NaFe_2PO_4(SO_4)_2$ for High Energy Sodium-Ion Batteries. Chemical Engineering Journal 2024, 493, 152485. https://doi.org/10.1016/j.cej.2024.152485.

(32) Essehli, R.; Alkhateeb, A.; Mahmoud, A.; Boschini, F.; Ben Yahia, H.; Amin, R.; Belharouak, I. Optimization of the Compositions of Polyanionic Sodium-Ion Battery Cathode $NaFe_{2-x}V_x(PO_4)(SO_4)_2$. J. Power Sources 2020, 469, 228417. https://doi.org/10.1016/j.jpowsour.2020.228417.

(33) Slater, P. R.; Greaves, C. Powder Neutron Diffraction Study of the Nasicon-Related Phases $Na_xM^{II}_xM^{III}_{2-x}(SO_4)_{3-y}(SeO_4)_y$: M^{II}=Mg, M^{III}= Fe, In. J. Mater. Chem. 1994, 4 (9), 1469–1473. https://doi.org/10.1039/JM9940401469.

(34) Hong, Y.-P. Crystal Structures and Crystal Chemistry in the System $Na_{1+x}Zr_2Si_xP_{3-x}O_{12}$. Mat. Res. Bull 1976, 11, 173–182. https://doi.org/10.1016/0025-5408(76)90073-8.

(35) Wu, Y.; Cao, Z.; Song, L.; Gao, J. $NaFe_2PO_4(MoO_4)_2$: A Promising NASICON-Type Electrode Material for Sodium-Ion Batteries. ACS Appl. Mater. Interfaces 2021, 13 (41), 48865–48871. https://doi.org/10.1021/acsami.1c15010.

(36) Petrícek, V.; Dušek, M.; Palatinus, L. Crystallographic Computing System JANA2006: General Features. Z. Kristallogr. 2014, 345–352. https://doi.org/10.1515/zkri-2014-1737.

(37) Toby, B. H.; Von Dreele, R. B. GSAS-II: The Genesis of a Modern Open-Source All Purpose Crystallography Software Package. J. Appl. Crystallogr. 2013, 46 (2), 544–549. https://doi.org/10.1107/S0021889813003531.

(38) Kraus, W.; Nolze, G. POWDER CELL-a Program for the Representation and Manipulation of Crystal Structures and Calculation of the Resulting X-Ray Powder Patterns. J. Appl. Crystallogr. 1996, 29, 301–303. https://doi.org/10.1107/S0021889895014920.

(39) Barpanda, P.; Chotard, J. N.; Recham, N.; Delacourt, C.; Ati, M.; Dupont, L.; Armand, M.; Tarascon, J. M. Structural, Transport, and Electrochemical Investigation of Novel AMSO$_4$F (A = Na, Li; M = Fe, Co, Ni, Mn) Metal Fluorosulphates Prepared Using Low Temperature Synthesis Routes. Inorg. Chem. 2010, 49 (16), 7401–7413. https://doi.org/10.1021/ic100583f.

(40) Reynaud, M.; Barpanda, P.; Rousse, G.; Chotard, J. N.; Melot, B. C.; Recham, N.; Tarascon, J. M. Synthesis and Crystal Chemistry of the NaMSO$_4$F Family (M = Mg, Fe, Co, Cu, Zn). Solid State Sci. 2012, 14 (1), 15–20. https://doi.org/10.1016/j.solidstatesciences.2011.09.004.

(41) Dwibedi, D.; Ling, C. D.; Araujo, R. B.; Chakraborty, S.; Duraisamy, S.; Munichandraiah, N.; Ahuja, R.; Barpanda, P. Ionothermal Synthesis of High-Voltage Alluaudite $Na_{2+2x}Fe_{2-x}(SO_4)_3$ Sodium Insertion Compound: Structural, Electronic, and Magnetic Insights. ACS Appl. Mater. Interfaces 2016, 8 (11), 6982–6991. https://doi.org/10.1021/acsami.5b11302.

(42) Olchowka, J.; Nguyen, L. H. B.; Petit, E.; Camacho, P. S.; Masquelier, C.; Carlier, D.; Croguennec, L. Ionothermal Synthesis of Polyanionic Electrode Material $Na_3V_2(PO_4)_2FO_2$ through a Topotactic Reaction. Inorg. Chem. 2020, 2020 (23), 17282–17290. https://doi.org/10.1021/acs.inorgchem.0c02546ï.

(43) Olchowka, J.; Fang, R.; Bianchini Nuernberg, R.; Pablos, C.; Carlier, D.; Cassaignon, S.; Croguennec, L. Particle Nanosizing and Coating with an Ionic Liquid: Two Routes to Improve the Transport Properties of $Na_3V_2(PO_4)_2FO_2$. Nanoscale 2022, 14 (24), 8663–8676. https://doi.org/10.1039/d2nr01080a.

(44) Minart, G.; Labrugère-Sarroste, C.; Weill, F.; Buffière, S.; Dourges, M. A.; Clermont, G.; Croguennec, L.; Olchowka, J. Ionic Liquid as a Template and a Carbon Source for Particle Engineering and Coating of $Na_3V_2(PO_4)_2F_{3-y}O_y$. J. Alloys Compd. 2025, 1018. https://doi.org/10.1016/j.jallcom.2025.179191.

(45) Kabbour, H.; Coillot, D.; Colmont, M.; Masquelier, C.; Mentré, O. α-$Na_3M_2(PO_4)_3$ (M = Ti, Fe): Absolute Cationic Ordering in NASICON-Type Phases. J. Am. Chem. Soc. 2011, 133 (31), 11900–11903. https://doi.org/10.1021/ja204321y.

(46) Hawthorne, F. C.; Krivovichev, S. V.; Burns, P. C. The Crystal Chemistry of Sulfate Minerals. Sulfate Minerals: Crystallography, Geochemistry, and Environmental Significance 2019, 40, 1–112. https://doi.org/10.2138/rmg.2000.40.1.

(47) Huminicki, D. M. C.; Hawthorne, F. C. The Crystal Chemistry of the Phosphate Minerals. In Phosphates: Geochemical, Geobiological and Materials Importance. Mineralogical Society of America 2019, 48, 123–254. https://doi.org/10.2138/rmg.2002.48.5.

(48) Gagné, O. C.; Hawthorne, F. C. Bond-Length Distributions for Ions Bonded to Oxygen: Results for the Transition Metals and Quantification of the Factors Underlying Bond-Length Variation in Inorganic Solids. IUCrJ. 2020, 7, 581–629. https://doi.org/10.1107/S2052252520005928.

(49) Menil, F. Systematic Trends of the ^{57}Fe Mössbauer Isomer Shifts in (FeO_n) and (FeF_n) Polyhedra. Evidence of a New Correlation between the Isomer Shift and the Inductive Effect of the Competing Bond T-X (-Fe) (Where X Is O or F and T Any Element with a Formal Positive Charge). J. Phys. Chem. Solids 1985, 46 (7), 763–789. https://doi.org/10.1016/0022-3697(85)90001-0.

(50) Beltrán-Porter, D.; Olazcuaga, R.; Fournès, L.; Ménil, F.; Le Flem, G.; Olazcuaga, R.; Foumes, L.; Menil, F.; Le Flem, G. Etude Magnétique et Par Résonance Mössbauer de l'orthophosphate $Na_3Fe_2(PO_4)_3$-α et d'une Phase Vitreuse Dérivée. Rev. Physique Appliquée 1980, 15 (6), 1155–1160. https://doi.org/10.1051/rphysap:019800015060115500ï.

(51) Idczak, R.; Tran, V. H.; Świątek-Tran, B.; Walczak, K.; Zając, W.; Molenda, J. The Effects of Mn Substitution on the Structural and Magnetic Properties of the NASICON-Type $Na_3Fe_{2-x}Mn_x(PO_4)_3$ Solid Solution. J. Magn. Magn. Mater. 2019, 491, 165602. https://doi.org/10.1016/j.jmmm.2019.165602.